RSC Advances

PAPER

Cite this: *RSC Adv.*, 2022, **12**, 16991

Novel Ta/chitosan-doped CuO nanorods for catalytic purification of industrial wastewater and antimicrobial applications

M. Ikram, *[a] A. Shahzadi,[b] S. Hayat,[c] W. Nabgan, *[d] A. Ul-Hamid, [e] A. Haider,[f] M. Noor,[c] Souraya Goumri-Said, [g] Mohammed Benali Kanoun[h] and S. Ali[c]

Received 12th May 2022
Accepted 30th May 2022

DOI: 10.1039/d2ra03006c

rsc.li/rsc-advances

Novel tantalum (Ta) and chitosan (CS)-doped CuO nanorods (NRs) were synthesized using a single step co-precipitation route. Different concentrations (2 and 4%) of Ta were used in fixed amounts of CS and CuO to examine their catalytic activity and antimicrobial potential. For critical analysis, synthesized NRs were systematically examined using XRD, FTIR HRTEM, EDS, UV-Vis and PL spectroscopy. The XRD technique revealed the monoclinic structure of CuO while an increase in its crystallite size (from 15.5 to 18.5 nm) was observed upon doping. FTIR spectra were examined to study the functional groups of CuO where peaks at 514 cm^{-1} and 603 cm^{-1} confirmed the formation of CuO NRs. PL spectra depicted the charge transfer efficiency of the synthesized samples. The presence of dopants (Ta and CS) and constituent elements (Cu, O) was detected using EDS spectra. Additionally, the pH based catalytic performance of fabricated NRs revealed 99.7% dye degradation of toxic methylene blue (MB) dye in neutral media, 99.4% in basic media and 99.5% in acidic media along with promising antibacterial activities for Gram negative/positive bacteria, respectively upon doping of Ta (4%) into CS/CuO. The adsorption energies of CuO co-doped with CS/Ta led to the creation of stable structures that were investigated theoretically using density functional theory.

1. Introduction

Water pollution has become a serious global concern due to the presence of agricultural pesticides, radiological and industrial discharge, and lack of proper treatment systems. Contaminated water is harmful to human health as well as the environment.[1–3] According to the published statistics, 1–4 million people die annually from water pollution and illnesses.[4] The large volume of waste from organic dyes originating from several industries results in significant environmental pollution.[5] For researchers, removal of toxins from polluted water and the atmosphere has become a major challenge in the last few decades.[6] To deal with this complex issue, many mechanical, physical, and chemical approaches such as adsorption[7,8] ozonation,[7] membrane filtration,[8] coagulation[1] ion exchange[9–11] bio adsorption,[12] photo catalytic degradation,[13,14] biological treatment[15] and catalytic reduction[16] have been used. Transition metal oxides (TMO) are a type of semiconductor that has many applications in magnetic storage devices, electronics, solar energy, photocatalysis and catalysis.[17] Different semiconducting materials such as MnO_2, SnO_2, CeO_2, CaO, ZnO and CuO have been extensively employed as catalysts. Among these semiconductors, CuO is one of the most promising p-type semiconductors due to its superior optical, magnetic and physical properties and is extensively employed in catalysis,[18] solar energy conversion,[19] photocatalysis, gas sensors,[20] as well as field emission.[21] Numerous approaches have been employed to fabricate CuO NRs of diverse shapes and dimensions in recent years including, sonochemical,[22] thermal oxidation,[23] combustion, sol–gel,[24] and co-precipitation methods.[25] Among these methods, co-precipitation has stimulated interest of the industry due to its relatively simple set-up, low energy and undemanding temperature requirements, as well as low cost and efficiency.

Chitosan (CS) has chelating characteristics and interacts with metal oxides including CS/ZnO, CS/TiO_2, CS/CdS and CS/Cu_2O, to remove dyes, poisonous organics, and antimicrobial

---

[a] *Solar Cell Application Research Lab, Department of Physics, Government College University Lahore, Lahore, 54000, Punjab, Pakistan. E-mail: dr.muhammadikram@gcu.edu.pk*

[b] *Faculty of Pharmacy, The University of Lahore, Lahore 54000, Pakistan*

[c] *Department of Physics, Riphah Institute of Computing and Applied Sciences (RICAS), Riphah International University, 14 Ali Road, Lahore, Pakistan*

[d] *Departament d'Enginyeria Química, Universitat Rovira i Virgili, Av Països Catalans 26, 43007, Tarragona, Spain. E-mail: wnabgan@gmail.com*

[e] *Core Research Facilities, King Fahd University of Petroleum & Minerals, Dhahran, 31261, Saudi Arabia. E-mail: anwar@kfupm.edu.sa*

[f] *Department of Clinical Sciences, Faculty of Veterinary and Animal Sciences, Muhammad Nawaz Shareef University of Agriculture, Multan, 66000, Pakistan*

[g] *College of Science, Physics Department, Alfaisal University, P. O. Box 50927, Riyadh 11533, Saudi Arabia*

[h] *Department of Physics, College of Science, King Faisal University, P. O. Box 400, Al-Ahsa, 31982, Saudi Arabia*

agents.[26–32] CuO combined with CS biopolymer can alter the basic metal oxide's biological characteristics. Because of its biocompatibility with biological systems and its nontoxicity, CuO has been widely employed in the food industry and biomedicine as an antioxidant in medication administration and particularly in antibacterial applications.[33] CS has a cationic architecture due to the presence of NH_2 and O–H groups, as well as positive charge caused by the presence of strong amino groups.[34,35] It may interact chemically with organic halogen, metal ions, and biomolecules.[36]

Transition metals doped inorganic semiconductors (SnO_2, MnO_2, ZnO, TiO_2 and CuO) exhibit important optical, morphological and magnetic properties.[37] Doping of transition metal tantalum (Ta) (2, 4%) in CuO decreased band gap and enriched optical characteristics of doped specimen and decreased E_g from 3.42 to 3.32 eV.[38] Ta is one of the most appealing materials owing to its broad band gap, high refractive index, large dielectric constant, piezoelectric characteristics, and mechanical stability at high temperatures (2, 3). Furthermore, Ta holds a lot of potential for use in biomedical field such as in coatings for medical applications and surgical tools, as well as for drug delivery, biosensors, and tissue engineering. In this study, co-precipitation approach was utilized to produce Ta/CS-doped CuO NRs for catalytic and antimicrobial applications. The synthesized NRs were used to purify industrial wastewater and remove organic compound namely methylene blue. Doping effect was analyzed by evaluating the optical, structural, and morphological of undoped and doped CuO NRs. The adsorption energies of CS on CuO surface and CS/Ta–CuO surface were calculated using density functional theory calculations.

2. Experimental section

2.1 Materials

Copper chloride ($CuCl_2\cdot 2H_2O$, 97%), chitosan ($(C_6H_{11}NO_4)_n$, 75–85%), sodium hydroxide (NaOH, 98%) and tantalum(V) chloride ($TaCl_5$, 99.8%) were acquired from Sigma-Aldrich (Germany).

2.2 Preparation of CuO

CuO nanostructures (NS) were synthesized through co-precipitation technique using copper chloride ($CuCl_2\cdot 2H_2O$). 0.5 M solution was prepared and heated at 80 °C under constant stirring. Afterward (0.1 M) solution of NaOH was used in the above colloidal solution to maintain pH = 12. Subsequently, colloidal solution was centrifuged for 6 minutes at 7500 rpm, then rinsed 2–3 times with DI water, and dried in oven at 100 °C for 10 hours. Finally, it was powdered to get CuO NRs in the form of black powder.[39]

2.3 Synthesis of Ta/CS-doped CuO

0.5 M of $CuCl_2\cdot H_2O$ was prepared and fixed amount of $C_6H_{11}NO_4$ (0.17 g) was added in the above prepared solution with continuous stirring at 80 °C to obtain colloidal solution. Afterward, various concentrations of $TaCl_5$ (2 and 4%) were poured into the solution and heated for 1 hour. Meanwhile, NaOH was used to retain pH = 12 and centrifuged at 7500 rpm for 6 minutes and washed several times with DI water. At the end, precipitates were dried at 100 °C for 10 hours to attain the final product (Fig. 1).

2.4 Catalytic study

Methylene blue (MB) was used to assess catalytic activity of pristine CuO and (2, 4%) Ta/CS-doped CuO in a solution containing a specific amount of $NaBH_4$ (400 μL, 800 μL) used as a reducing agent in basic, acidic and neutral medium. NRs were added into the solution containing MB and reducing agent, which resulted in substantial degradation. UV-Vis absorption measurements ranging from 200 to 800 nm were used to record the degree of dye degradation.[40,41]

2.5 Antibacterial activity

The antimicrobial behavior of produced (2, 4%) Ta/CS-doped CuO NRs was revealed using virulent *Staphylococcus aureus* (*S. aureus*) and *Escherichia coli* (*E. coli*) bacteria in a well diffusion test. Microbial growth was observed on mannitol sodium acetate (MSA) and MacConkey agar (MCA). On MSA and MCA plates cultured with 0.5 McFarland bacteria growth, wells with an interior diameter of about 6 mm were bored using autoclaved borer.[40,42] Petri dishes were then incubated for 24 hours at 37 °C, and inhibited zones around wells were recorded. The ranges of the inhibition regions around the wells (in mm) reflected the extent of antibacterial activity. Ciprofloxacin (0.005 mg/50 μL) was employed as the standard antibiotic, while DIW (50 μL) was used as the control negative in comparison to different concentrations of synthesized NRs (0.5 and 1.0 mg/50 μL) as least and maximal dosages, accordingly. The plates were inoculated aerobically overnight at 37 °C, and the inhibition areas were determined using a Vernier caliper.[43]

2.6 Characterization

Crystalline structure along with phase constitution of materials was characterized with XRD using Bruker XRD, D2 Phase, equipped with (Cu-Kα) radiation. Fourier-transform infrared (FTIR) Perkin Elmer 4000 spectrophotometer was used for chemical analysis and to confirm the presence of related functional groups during synthesis. Absorption spectra in the 200–700 nm wavelength range were measured with UV-Vis spectroscopy (Genesys 10S). Using a spectrofluorometer (JASCO, FP-8300), PL spectra were acquired to investigate the migration and electron–hole pair recombination. HR-TEM (JEOL JEM 2100F) and FESEM JSM-6460LV equipped with an Oxford EDS spectrometer were used to analyze the shape and *d*-spacing of fabricated specimen.

3. Results and discussion

To investigate structural properties, crystalline size as well as phase formation of CuO and Ta/CS-doped CuO NRs, XRD was employed in the 2θ range of 10°–80° as depicted in Fig. 2a. The characteristic peaks were noticed at $2\theta^\circ = 32.33^\circ, 35.47^\circ, 38.61^\circ,$

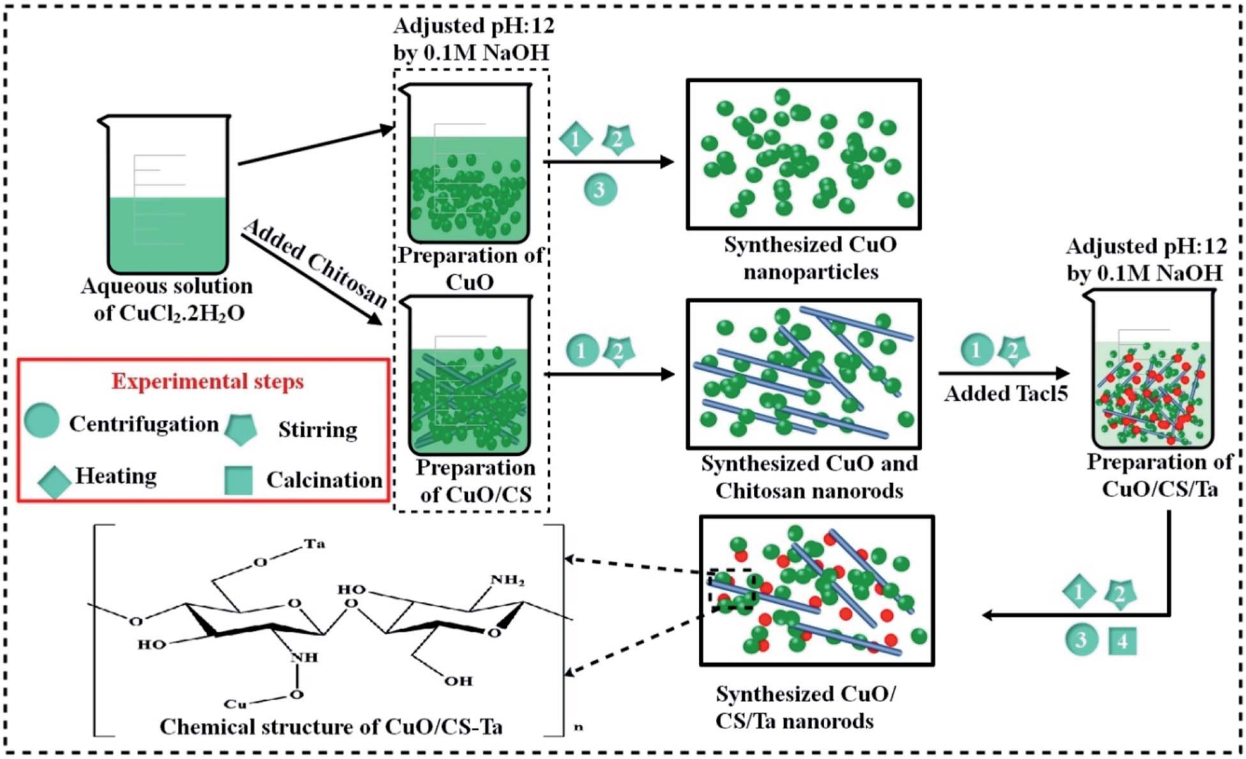

Fig. 1 Schematic diagram of synthesis of Ta/CS–CuO NRs.

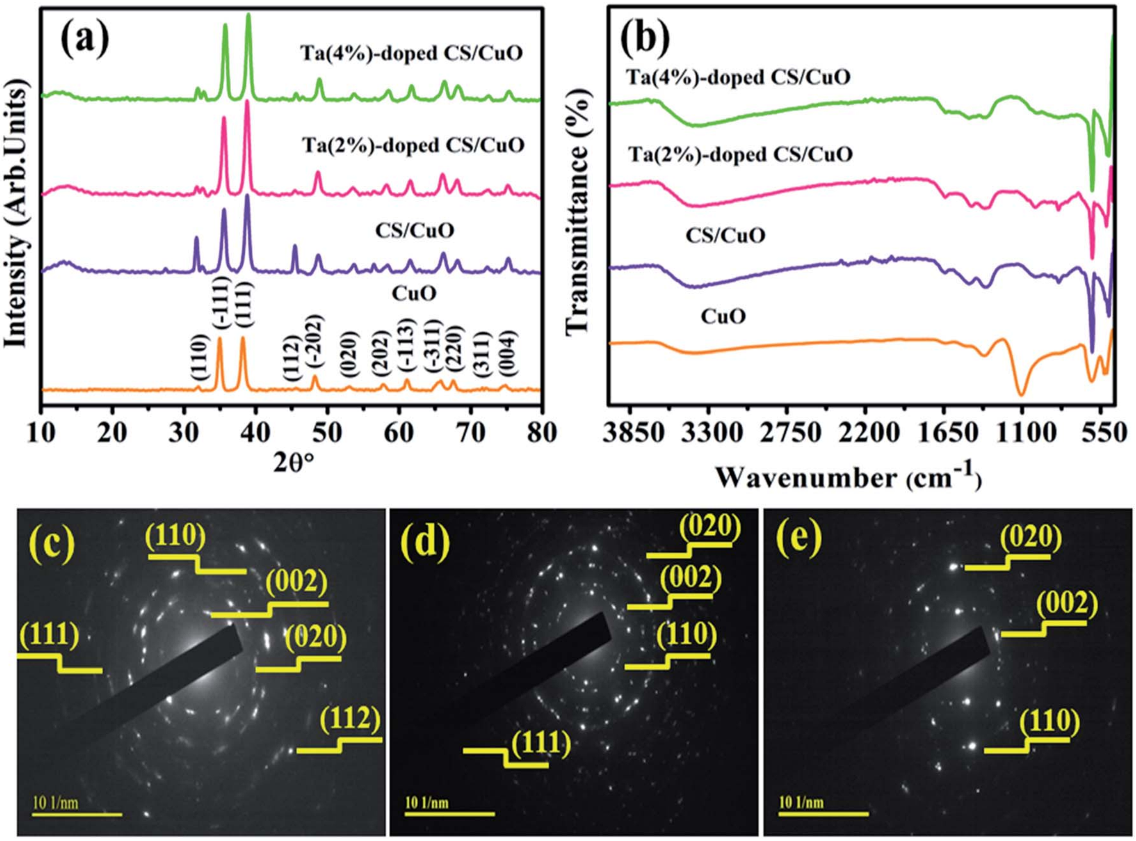

Fig. 2 (a) XRD pattern and (b) FTIR spectra and (c–e) SAED patterns of pristine and (2, 4%) Ta/CS-doped CuO NRs.

45,55°, 48.64°, 53.30°, 58.02°, 61.42°, 66.16°, 67.85°, 72.20° and 74.89° corresponding to (110), (−111), (111), (112), (−202), (020), (202), (−113), (−311), (220), (311) and (004) planes of monoclinic CuO, respectively (JCPDS no. 05-0661/01-078-2076).[44] As shown in Fig. 2a, the peak detected around 13.01° confirmed the presence of CS in CuO.[26] Additionally, peaks related to impurities such as $TaCl_2$ and Ta_2O_5 or other crystalline impurities were not found in tested samples, indicating high-level of purity of prepared specimens. Furthermore, upon addition of CS and Ta in CuO, peaks slightly moved towards the higher diffraction angle. This shift may be due to the size of the Ta^{5+} ionic radii (0.64 Å) that is less than the ionic radii of CuO (0.73 Å) while Ta^{5+} ions are more likely to be absorbed into the CuO lattice at low concentrations of Ta^{5+}, making it easier to replace CuO lattice site.[45] The crystallite size of all concerned samples was found to be 15.5, 15.9, 24.8 and 18.6 nm, respectively using Debye–Scherrer's equation.[46]

FT-IR was used to examine the functional groups and related vibrational modes in CuO and Ta/CS-doped CuO NRs. Fig. 2b shows high-frequency modes at 514 and 604 cm^{-1}, respectively due to Cu–O stretching vibrations.[44,47] The band found at ∼1350 cm^{-1} revealed C–N stretching mode of amide group.[48] Peak flexing at ∼1631 cm^{-1} was attributed to amide group (CONH–), meanwhile, peak at ∼1116 cm^{-1} verified (O–H) stretching.[49] The band at 3450 cm^{-1} showed anti-symmetric stretching vibrations of O–H bonds.[50] The absorption peak at ∼2122 cm^{-1} in CS-doped CuO was mainly attributed to vibration absorption of –C═CH group.[51] Peak noticed at ∼2335 cm^{-1} was designated to stretching vibration of adsorbed CO_2.[52] Subsequently, selected area electron diffraction (SAED) images for CuO, CS/CuO and (2, 4%) Ta/CS-doped CuO (Fig. 2c–e) revealed crystalline nature of as-synthesized NRs with indexed spots at (002), (020), (110), (111) and (112) planes that agreed with XRD data thus confirming the monoclinic structure of CuO.

Optical properties of CuO NRs with different doping concentrations were studied using UV-Vis spectroscopy ranging from 200–800 nm (Fig. 3a). The CuO peak with high intensity at ∼362 nm, unveiled the electronic transition from n–π* molecular orbitals of the region.[53,54] However, upon CS doping in CuO, absorbance peak shift toward the lower wavelength (blueshift) was observed, which is mainly due to surface plasmon resonance (SPR).[55] In addition, upon adding of 2, 4% Ta in CS/CuO redshift was noted may be caused by imperfection states, impurities and p–d electrons interaction between metal ions and oxygen produced by Ta dopant as visualized in Fig. 3a.[56,57] The E_g of NRs was extracted from absorption spectra through Tauc plot with corresponding results (Fig. 3b). Calculated E_g of CuO, CS/CuO, (2, 4%) Ta-doped CS/CuO was 3.4, 4.5, 3.32 and 3.29 eV, respectively.[44] The decrement in E_g may be due to defects created in the crystal structure by incorporation of different metal ions.[58]

Photoluminescence (PL) spectra were acquired to explore optical properties, variation in electron transfer efficiency and

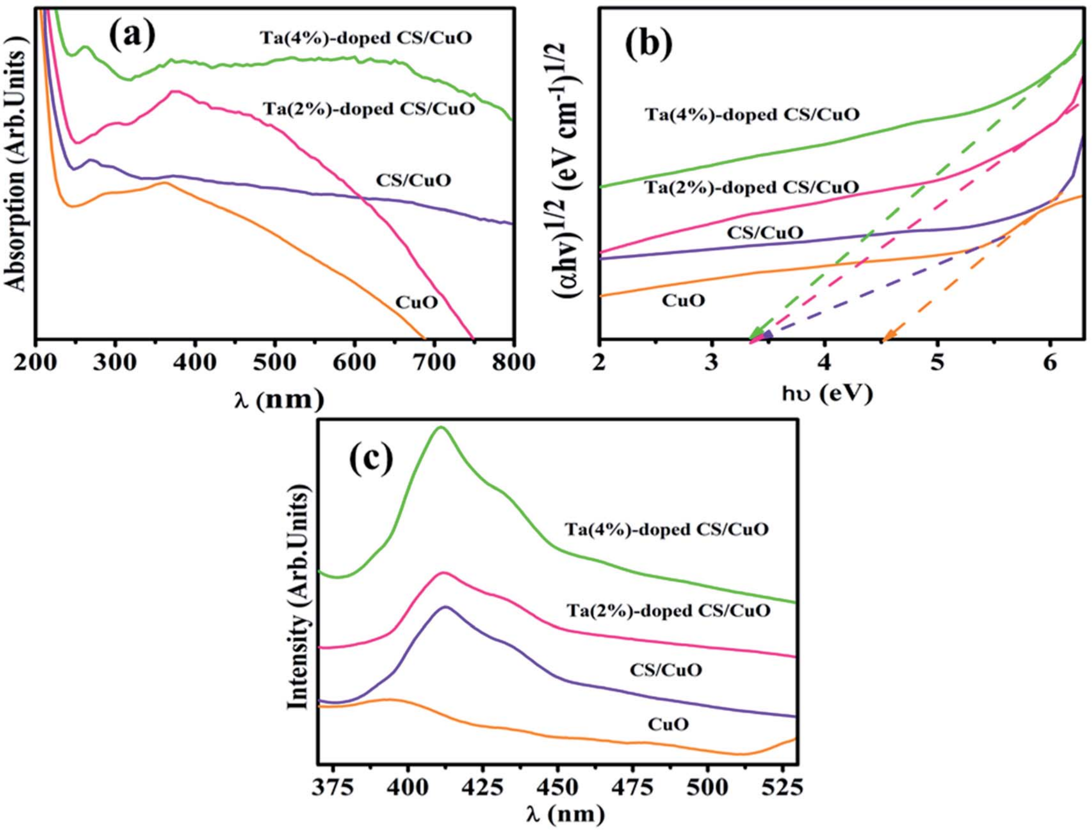

Fig. 3 (a) Absorption spectra (b) calculated E_g and (c) PL spectra of pristine and (2, 4%) Ta/CS-doped CuO.

recombination rate of excited electrons and holes as shown in Fig. 3c.[59] The visible emission peak at ~391 nm which is related to violet region corresponded to CuO NRs with adjacent band emission and is well consistent with absorption measurements.[59] In pristine CuO spectrum, slight hump of blue band luminescence at ~488 nm may be caused by interstitial oxygen and transition oxygen vacancy.[59,60] However, doping of (2, 4%) Ta in CS/CuO NRs demonstrated high recombination rate of (e^-–h^+) pairs and less efficiency of electron transfer.[42]

High resolution TEM analysis revealed detailed morphological information about as-prepared materials morphology. HR-TEM micrographs of CuO and (2, 4%) Ta/CS-doped CuO are presented in Fig. 4. Figure exhibits nanorods-like morphology of as-synthesized pure sample. Fig. 4b–d revealed agglomeration of CS and Ta-doped samples and also shows self-aggregation of nanorods. From HR-TEM images of CuO, CS/CuO and with 2, 4% Ta-doped CuO NRs (Fig. 4a′–d′), *d*-spacing was calculated and found to be 0.27, 0.25, 0.23 and 0.24 nm, respectively which corresponded to (110), (−111), (111) and (112) planes of CuO and is well consistent with XRD data (JCPDS no. 05-0661/01-078-2076). Gatan software was used to calculate *d*-spacing for each specimen (Fig. 4a′–d′).

Micrographs obtained from scanning electron microscopy (FE-SEM) analysis unveiled the surface morphological features of dopant-free CuO, CS/CuO, and (2 and 4%) Ta/Cs co-doped CuO as manifested in Fig. 5a–d, respectively. FE-SEM results indicate the evolution of nanorods (NRs) of CuO, meanwhile the morphology of (2%, and 4%) Ta/CS co-doped CuO is divulged in Fig. 5b–d. The images of NRs doped with 4% Ta/CS concentration exhibited highly agglomerated NRs as expressed in Fig. 5d.

To ascertain the chemical elements of prepared samples, SEM-EDS was used (Fig. 6a–d).[21] Strong peaks of Cu and O verified the successful formation of CuO, whereas CS and Ta peaks in the doped samples showed that CS and Ta atoms have been effectively doped in the lattice of CuO. The pristine sample has Na peaks that could be due to the NaOH used to control the

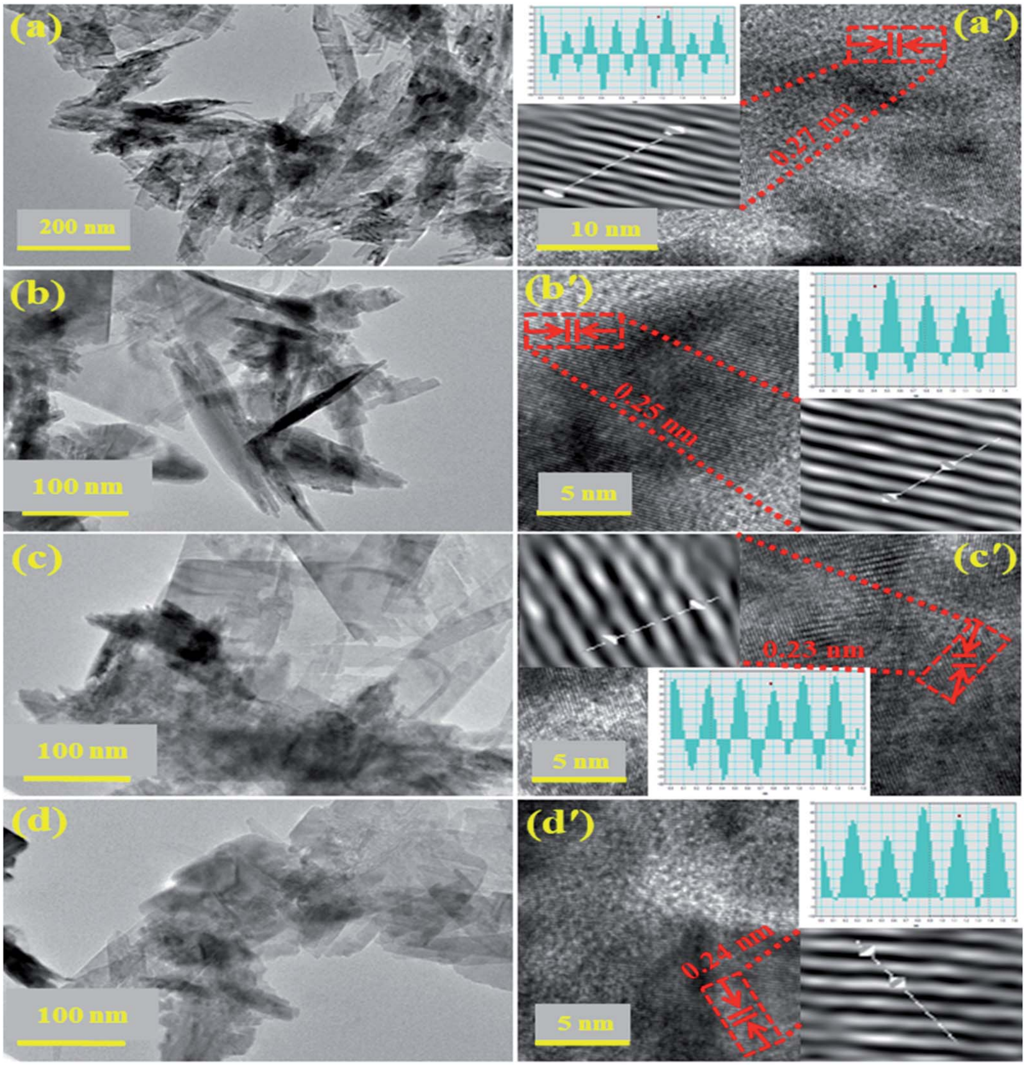

Fig. 4 (a–d) HR-TEM micrographs of pristine CuO and Ta/Cs-doped CuO, respectively; (a′–d′) interlayer *d*-spacing of CuO and co-doped NRs, respectively.

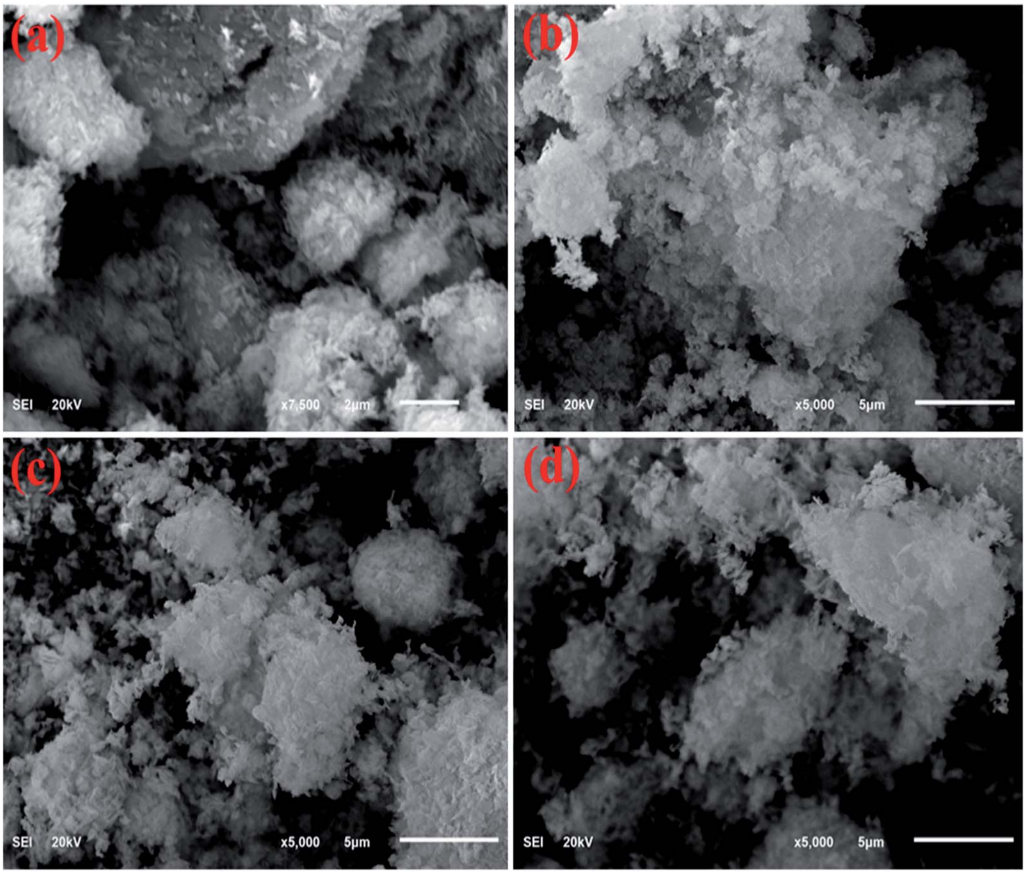

Fig. 5 (a–d) SEM analysis of dopant-free CuO, CS/CuO and (2 and 4%) Ta/Cs co-doped CuO, respectively.

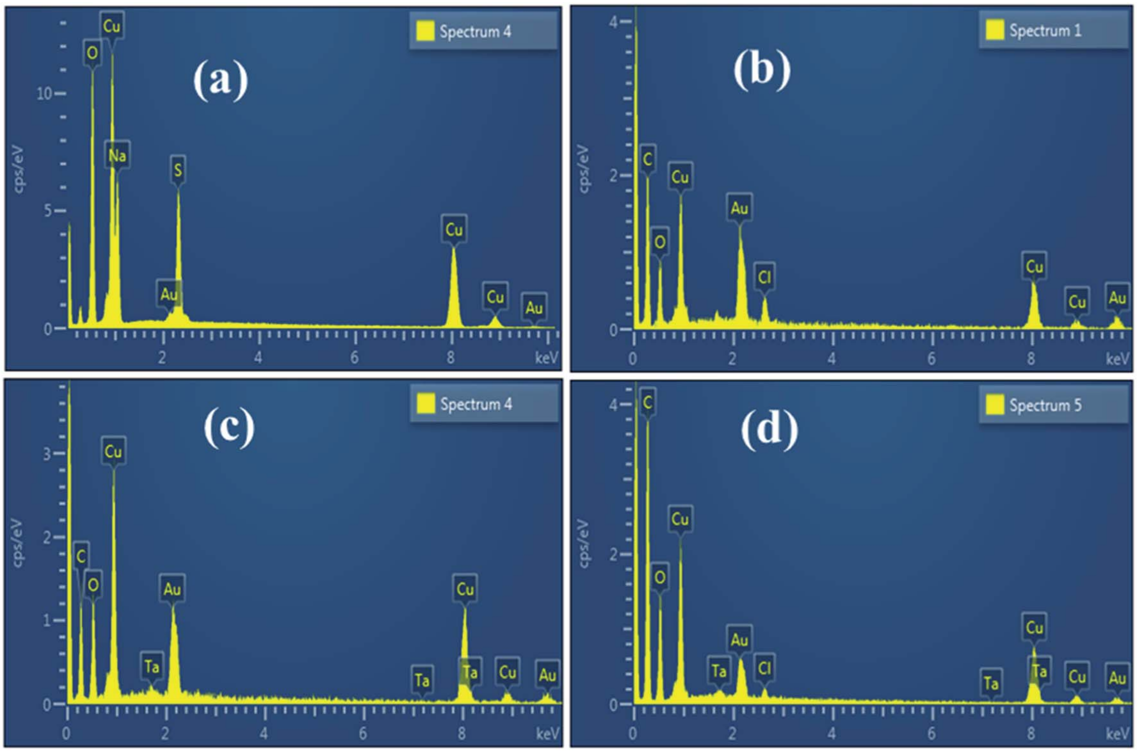

Fig. 6 (a) EDS spectra of pristine (b) CS/CuO and (c and d) (2, 4%) Ta/CS-doped CuO.

pH during synthesis. The gold coating on the samples reduces the charging effect, giving rise to Au peaks in the spectra.

3.1 Antimicrobial activity

In the context of *S. aureus* and *E. coli* microorganisms, bactericidal potency was investigated as presented in Table 1, illustrating inhibition areas for CuO, CS/CuO and (2%, 4%) Ta/CS-doped CuO NRs. The results indicated synergistic response due to various concentrations of doped CuO NRs. Substantial inhibition areas were measured against *S. aureus* and *E. coli* ranges of 3.15–7.35 nm and 2.50–4.20 nm (high dosage), respectively for doped CuO. Ta/CS-doped CuO with 4 wt% doping concentration showed increased bactericidal effectiveness against *S. aureus* compared to *E. coli*. Ciprofloxacin (control +ve) revealed diameters of 4.35 and 5.35 nm towards *S. aureus* and *E. coli*, respectively. Upon use of higher concentration of Ta, the results showed a significant increase in zone diameter, indicating improved bactericidal activity. Proposed antimicrobial mechanism is shown in Fig. 7.

Table 1 Bactericidal response of Ta/CS-doped CuO NRs

	[a]Inhibition region (mm)		[b]Inhibition region (mm)	
Specimen	0.5 mg/50 μL	1.0 mg/50 μL	0.5 mg/50 μL	1.0 mg/50 μL
CuO	1.35	2.25	4.25	4.40
CS/CuO	1.95	2.50	2.25	3.15
Ta (2%) : CS : CuO	2.65	3.45	3.35	5.20
Ta (4%) : CS : CuO	3.80	4.20	4.40	7.35
Ciprofloxacin	5.35	5.35	4.35	4.35
DIW	0	0	0	0

[a] Measurement of inhibition region for G −ve. [b] Inhibition areas (mm) against G +ve.

XPS was utilized to evaluate the surface elemental configuration, surface state, and binding energy changes of Ta/CS-doped CuO NRs Fig. 8a–d. The high-resolution spectra of O 1s, Ta 4f, and Cu 2p are illustrated in Fig. 8a–d. The prominent BE peak at 531.9 eV in Fig. 6a is attributed to surface –OH groups in the O 1s spectrum of Ta.[61] The Fig. 8b demonstrates the O 1s peak fitting spectra of CuO, which precisely reveals the distinct influence of oxygen with binding energies of 530.9 and 532.3 eV, correspondingly, for (C–OH) and (C–O–C).[62] The Ta 4f configuration at 21.5 and 23.4 eV corresponds to Ta 4f$_{7/2}$ and Ta 4f$_{5/2}$, respectively, implying sample metallic crests, as illustrated in Fig. 8c.[63] The Cu^{2+} core level apex fitting spectra has a significant peak at 933.3 eV, which coincides with core level of Cu 2p$_{3/2}$, as depicted in Fig. 8d, confirming the synthesis of two valence copper oxide NRs. Three higher spectra at 935.8, 941.1, and 943.6 eV are projected to impede satellite heights.[64]

3.2 Catalytic activity

The dye degradation (MB) for catalysis of pure and (2, 4%) Ta/CS-doped CuO was studied using UV-Vis spectroscopy (Fig. 9). The bare and co-doped NRs showed the maximum degradation (90, 99.1, 99.6 and 99.7%) in neutral medium (pH = 7), (7, 83.1, 99 and 99.4%) in basic (pH = 12), and (99.2, 98.3, 99.4 and 99.4%) in acidic medium (pH = 4). In all mediums, 4% Ta/CS-doped CuO exhibited the highest catalytic activity (Fig. 9a–c). The crystalline structure, geometry, and surface area of NRs have an impact on the catalytic study of these materials. Generally, maximum catalytic efficiency was observed when the surface area of the catalytic was large, since it provided more active sites. Catalytic efficiency increases in acidic medium due to an increase in the formation of H$^+$ ions obtained to absorb

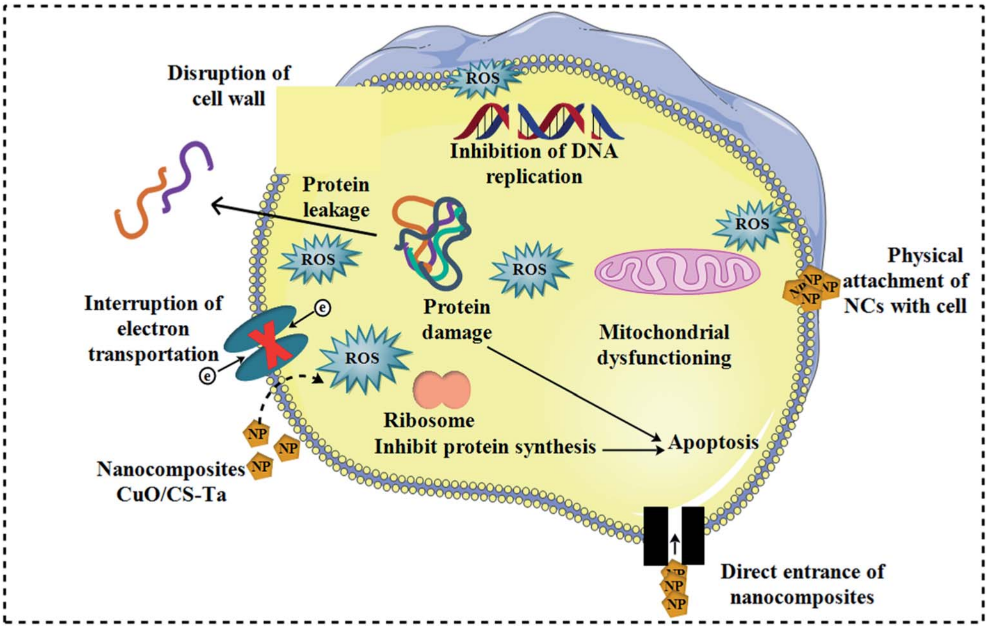

Fig. 7 Schematic diagram of proposed antimicrobial mechanism.

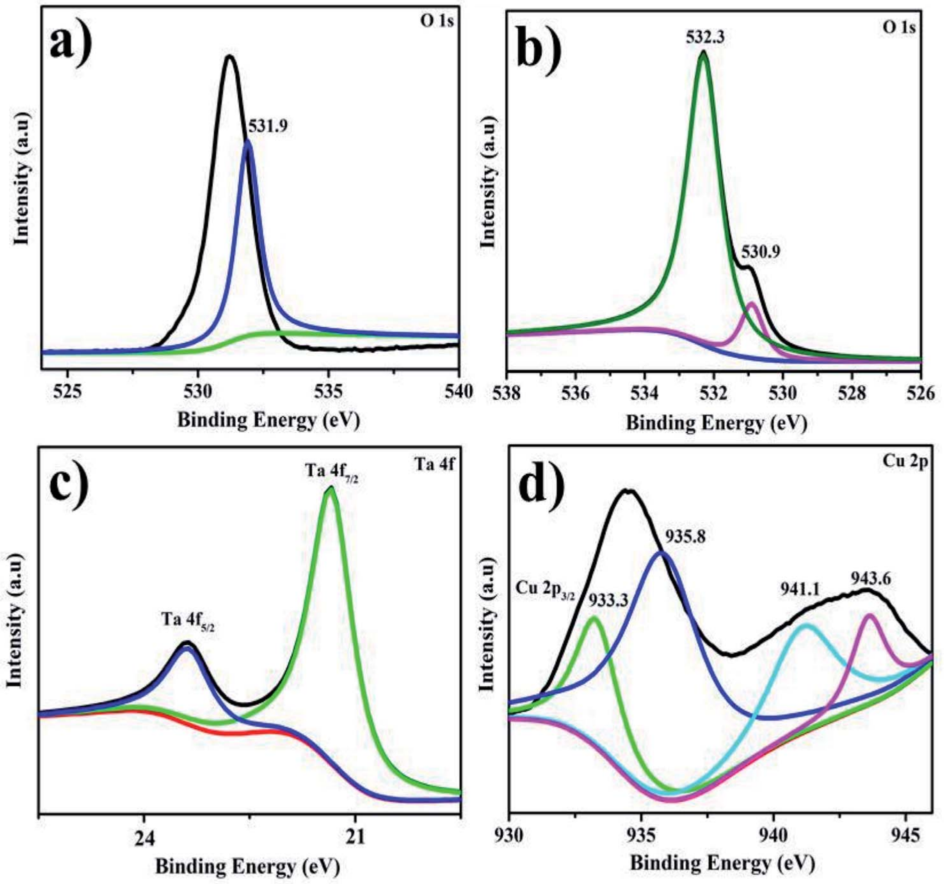

Fig. 8 XPS spectra of doped CuO NRs (a) O 1s spectra of Ta (b) and CuO (c) Ta 4f (d) Cu 2p.

NRs surface. In basic medium, increase in the number of –OH groups leads to the oxidation of reduced products and reduction in catalytic effectiveness.[40,65]

The dye degradation phenomenon is well explained in Fig. 10. After the breakdown of NaBH$_4$, BH$_4^-$ becomes an electron donor, transferring electrons to dye MB *via* CuO, CS/CuO and (2%, 4%) Ta/CS-doped CuO NRs. During MB dye degradation, the most of crucial part is played by (4%) Ta/CS-doped CuO NRs, which accept the electrons and then transfer these electrons.[60,61] Reduction in redox potential may occur which increase in Fermi potential, and which probably is affected by the size of NRs.[7] The size of NRs plays a key role in determining the nature of interfacial potential-barrier, for small particles barrier is small since surface is larger, and *vice versa*.[7] In this study, efficiency as well as catalysis speed was assessed and found to increase from reference CuO to CS/CuO, (2%) Ta/CS@CuO and (4%) Ta/CS@CuO samples, respectively. This happens because size reduction or increase has inverse dependence upon Ta concentration *i.e.*, high concentration of Ta decreases particle size or in contrast by lowering concentration increases size and *vice versa*.[62]

As catalytic stability is an essential factor for catalyst performance, recycling and stability of executed experiment was measured. For concerned samples, the performed experiment was stayed for almost 3 days after UV light exposure for 80 minutes. It was noted that degradation as well as discoloration were still the same as seen in the initial form. Recycling experiment was investigated with recycling of (4%) Ta/CS co-doped CuO only because this divulged promising result for dye degradation as compared to the rest of the prepared specimens as presented in Fig. 11. This experiment was performed up to 4 cycles; which revealed almost the same result as of the actual experiment.

3.3 Theoretical calculations

To gain an in-depth understanding of the catalytic activity in Ta/CS doped CuO, we carried out first-principles density functional theory computations within the Perdew, Burke, Ernzerhof (PBE) generalized gradient approximation (GGA)[66] for exchange–correlation energy functional, as implemented in the Quantum Atomistix ToolKit (QuantumATK) code.[67] For simulation, the PseudoDojo-medium norm-conserving pseudopotential[68] and cut-off energy of 10^5 Ha were employed. A $4 \times 3 \times 1$ *k*-point mesh constructed by the Monkhorst–Pack grid method was used to sample the Brillouin region. To account for the high correlations, GGA + *U* calculations were carried out using a Hubbard parameter, *U*, with an effective value ($U_{\text{eff}} = 7$ eV) for the appropriate description of the Cu 3d electrons.[69,70] The CuO surface was built from the optimized geometry bulk CuO

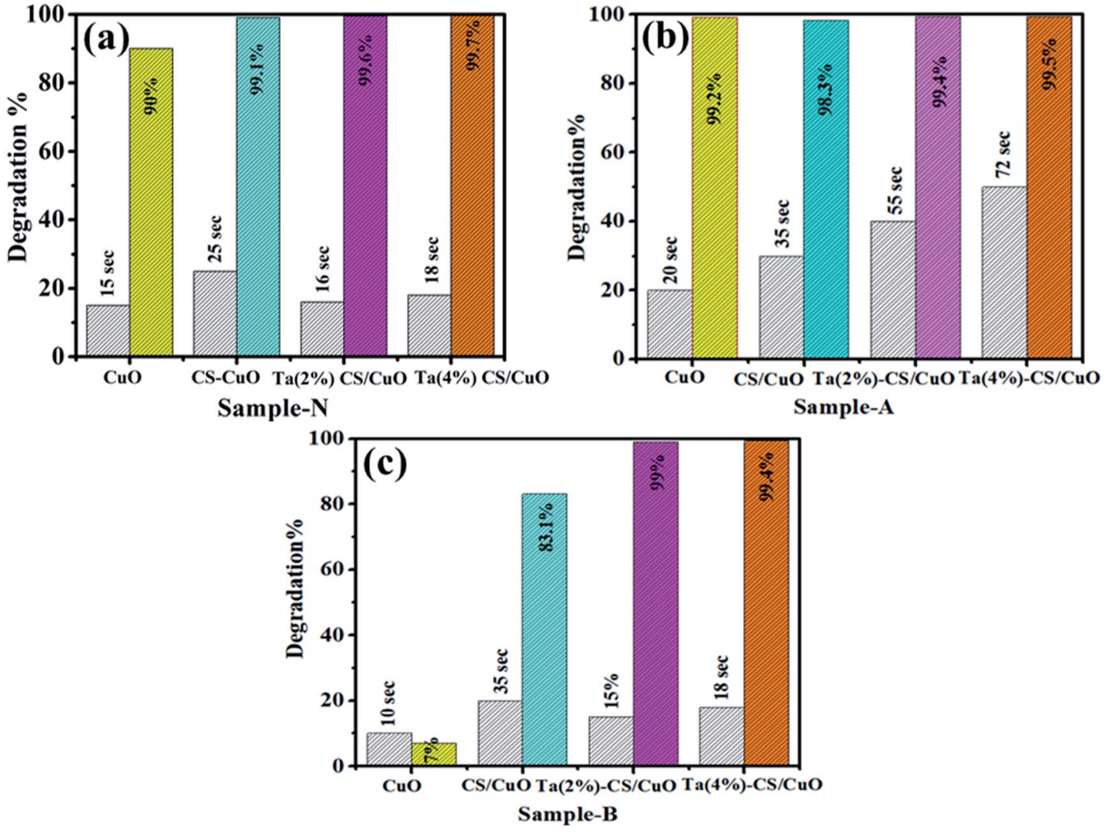

Fig. 9 Catalysis of pristine, CS/CuO, Ta/CS-doped CuO in (a) neutral (b) acidic and (c) basic medium.

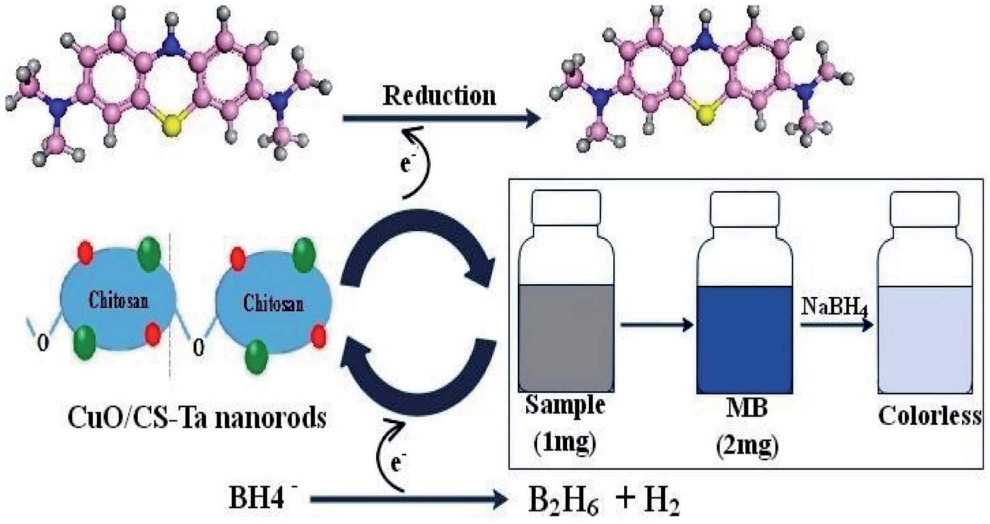

Fig. 10 Schematic diagram of catalysis mechanism.

structure with the lattice constants of $a = 4.455$ Å, $b = 3.821$ Å, $c = 5.175$ Å and $\beta = 92.29°$, which agree well with theoretical values and experimental measurements.[44,69–71] Because CuO surface along (111) orientation represents the most stable configuration, it was selected as the model for simulating CS adsorption[69] A slab containing of three layers with (4 × 3) supercell size is used to construct the CuO (111) surface (Fig. 12a). A 15 Å vacuum layer was applied between two adjacent slabs to exclude spurious effects owing to periodic boundary condition. The plot of Fig. 12a shows that the upper layer makes up two types Cu and O atoms containing coordinatively unsaturated and coordinatively saturated atoms. However, the coordinatively unsaturated surface oxygen (O_{3SUF}) atom is connected to one coordinatively unsaturated subsurface

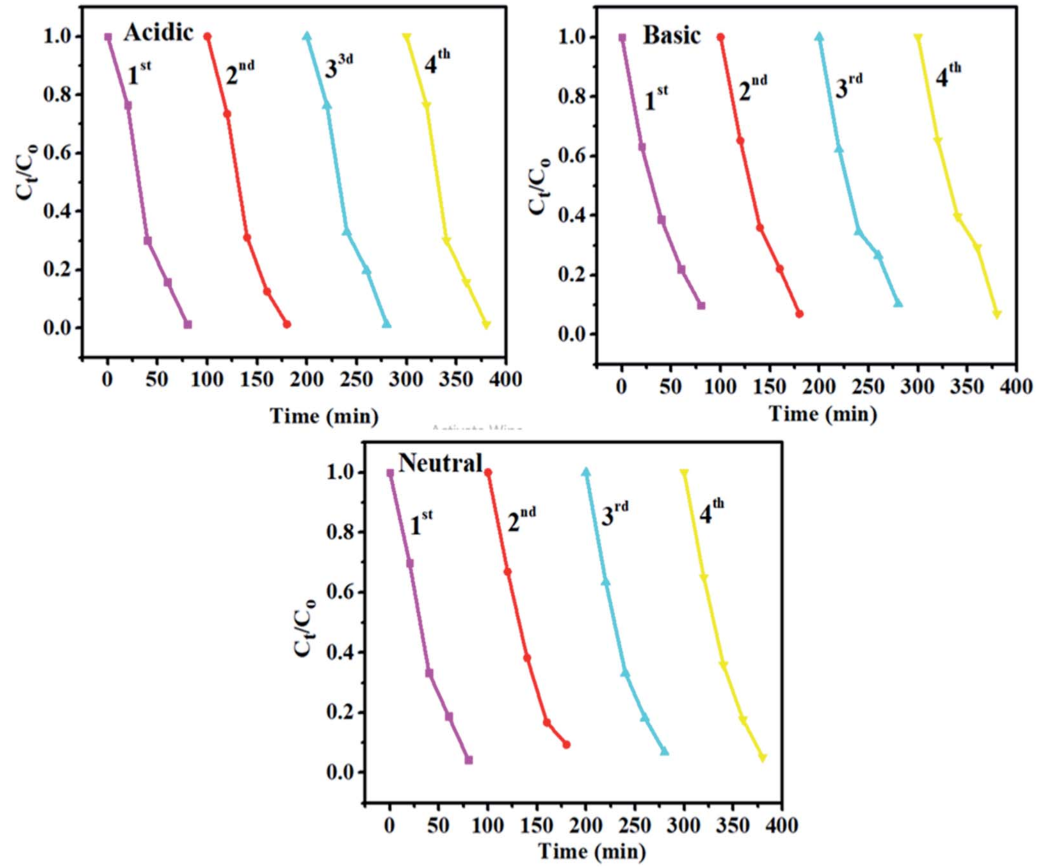

Fig. 11 The plots for C_t/C_o *vs.* time for the recycling of catalytic activity of (4%) Ta/CS co-doped CuO.

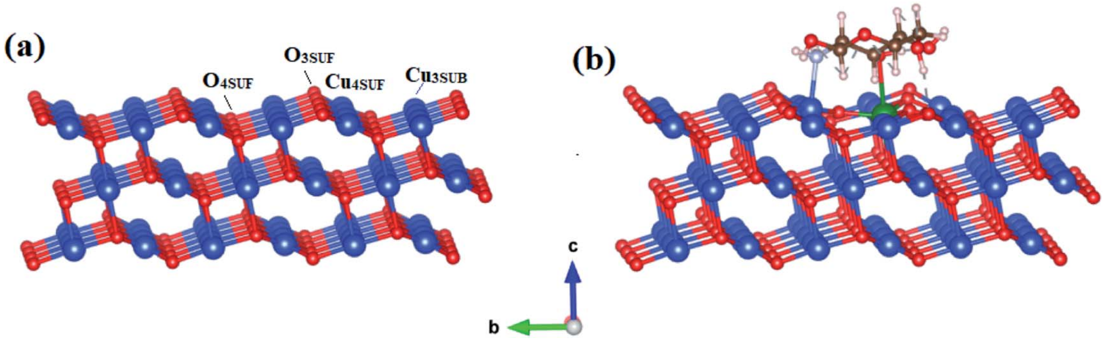

Fig. 12 The optimized structures (a) CuO (111) surface; (b) CS/Ta doped CuO (111) surface (red: O; blue: Cu; green: Ta; brown: C; light blue N; gray: H).

cooper (Cu_{3SUB}) atom and two coordinatively saturated surface (Cu_{4SUF}) atoms. Moreover, subsurface O_{4SUB} atom is linked to two Cu_{4SUF} atoms on both sides, one Cu_{3SUB} atom, and one Cu_4 atom corresponding to the second layer. Cu_{3SUB}–O_{3SUF} bond length is 1.870 Å, while Cu_{3SUB}–O_{4SUF} bond length is 1.942 Å, both of which are significantly less than the Cu–O bond length of 1.964 Å in bulk structure. Cu_{4SUF} and O_{4SUB} have lengths of 1.987 Å and 1.985 Å, respectively, and Cu_{4SUF}–O_{3SUF} has a distance of 1.952 Å, which is larger than the Cu–O bond length (1.964 Å) in bulk structure.

The interaction strength of CS and CuO surface as well as Ta-doped CuO surface is defined by the magnitude of adsorption energy, which is determined using the equation below:[72,73]

$$E_{\text{ads}} = E_{\text{molecule+slab}} - E_{\text{slab}} - E_{\text{molecule}} \tag{1}$$

where $E_{\text{molecule+slab}}$, E_{slab}, and E_{molecule} represent the overall energies of the surface and adsorbed molecule complex, as well as the energy of a clean surface slab and an isolated molecule, respectively. Surface optimization was also achieved by relaxing the two upper layers and maintaining the bulk state of the bottom layer. According to this concept, a negative adsorption energy value indicates a steady adsorption. After optimization, the adsorption energies of CS on the CuO (111) surface and CS/Ta on the CuO (111) surface are −1.26 eV and −1.79 eV, respectively. Both negative values of adsorption energy show that two complexes are favorable thermodynamically. The bond distance of N–Cu_{3SUB} is 2.321 Å for CS on the CuO (111) surface, whereas the N–Cu_{3SUB} bond length is reduced to 2.237 Å in the CS/Ta–CuO (111) surface (Fig. 12b).

4. Conclusion

In this study, the co-precipitation approach was used to effectively synthesize pristine and co-doped CuO NRs while the obtained NRs were evaluated for efficient catalytic degradation of MB. Bactericidal performance of synthesized material was also evaluated. The effects of Ta and CS dopants on phase constitution, optical properties, surface morphology and elemental composition of (2, 4%) Ta/CS-doped CuO were studied. XRD analysis revealed that NRs have a monoclinic structure whereas crystallite size increased from 15.5 to 18.6 nm upon addition of co-dopants while the presence of CuO and functional groups was confirmed with EDS and FTIR results, respectively. Decrease in E_g from 3.4 to 3.32 eV was recorded for 4% Ta/CS-doped samples. Chemical composition was calculated with EDS which confirmed the presence of constituent elements Cu, O, Ta, S, Na. In comparison to pristine and CS/CuO, co-doped samples showed the maximum degradation performance against MB dye (*i.e.*, 99.4–99.7%). The creation of stable structures was investigated using a theoretical research based on density functional theory to analyze the adsorption properties of the CS/Ta on CuO surfaces.

Data availability

Data would be made available on demand.

Conflicts of interest

There are no conflicts to declare.

Acknowledgements

NRPU Project 20-17615 from HEC, Pakistan is much appreciated by the authors. The Core Research Facilities, KFUPM in Dhahran, Saudi Arabia has been a tremendous help.

References

1 M. Ikram, A. Mahmood, A. Haider, S. Naz, A. Ul-Hamid, W. Nabgan, I. Shahzadi, J. Haider, I. Ahmad and S. Ali, Dye degradation, antibacterial and in-silico analysis of Mg/cellulose-doped ZnO nanoparticles, *Int. J. Biol. Macromol.*, 2021, **185**, 153–164, DOI: 10.1016/j.ijbiomac.2021.06.101.

2 Y. Zhang, B. Wu, H. Xu, H. Liu, M. Wang, Y. He and B. Pan, Nanomaterials-enabled water and wastewater treatment, *NanoImpact*, 2016, **3–4**, 22–39, DOI: 10.1016/j.impact.2016.09.004.

3 V. Gitis and N. Hankins, Water treatment chemicals: trends and challenges, *J. Water Process. Eng.*, 2018, **25**, 34–38, DOI: 10.1016/j.jwpe.2018.06.003.

4 B. C. Hodges, E. L. Cates and J. H. Kim, Challenges and prospects of advanced oxidation water treatment processes using catalytic nanomaterials, *Nat. Nanotechnol.*, 2018, **13**, 642–650, DOI: 10.1038/s41565-018-0216-x.

5 N. J. Vickers, Animal Communication: When I'm Calling You, Will You Answer Too?, *Curr. Biol.*, 2017, **27**, R713–R715, DOI: 10.1016/j.cub.2017.05.064.

6 A. Rafiq, M. Ikram, S. Ali, F. Niaz, M. Khan, Q. Khan and M. Maqbool, Photocatalytic degradation of dyes using semiconductor photocatalysts to clean industrial water pollution, *J. Ind. Eng. Chem.*, 2021, **97**, 111–128, DOI: 10.1016/j.jiec.2021.02.017.

7 K. H. Hama Aziz, H. Miessner, S. Mueller, A. Mahyar, D. Kalass, D. Moeller, I. Khorshid and M. A. M. Rashid, Comparative study on 2,4-dichlorophenoxyacetic acid and 2,4-dichlorophenol removal from aqueous solutions *via* ozonation, photocatalysis and non-thermal plasma using a planar falling film reactor, *J. Hazard. Mater.*, 2018, **343**, 107–115, DOI: 10.1016/j.jhazmat.2017.09.025.

8 Z. Li, G. Wang, K. Zhai, C. He, Q. Li and P. Guo, Methylene blue adsorption from aqueous solution by loofah sponge-based porous carbons, *Colloids Surf., A*, 2018, **538**, 28–35, DOI: 10.1016/j.colsurfa.2017.10.046.

9 A. Nezamzadeh-Ejhieh and M. Kabiri-Samani, Effective removal of Ni(II) from aqueous solutions by modification of nano particles of clinoptilolite with dimethylglyoxime, *J. Hazard. Mater.*, 2013, **260**, 339–349, DOI: 10.1016/j.jhazmat.2013.05.014.

10 A. Nezamzadeh-Ejhieh and M. Karimi-Shamsabadi, Decolorization of a binary azo dyes mixture using CuO incorporated nanozeolite-X as a heterogeneous catalyst and solar irradiation, *Chem. Eng. J.*, 2013, **228**, 631–641, DOI: 10.1016/j.cej.2013.05.035.

11 H. Shirzadi and A. Nezamzadeh-Ejhieh, An efficient modified zeolite for simultaneous removal of Pb(II) and Hg(II) from aqueous solution, *J. Mol. Liq.*, 2017, **230**, 221–229, DOI: 10.1016/j.molliq.2017.01.029.

12 M. Anari-Anaraki and A. Nezamzadeh-Ejhieh, *Modification of an Iranian clinoptilolite nano-particles by hexadecyltrimethyl ammonium cationic surfactant and dithizone for removal of Pb(II) from aqueous solution*, Elsevier Inc., 2015, DOI: 10.1016/j.jcis.2014.11.017.

13 H. Derikvandi and A. Nezamzadeh-Ejhieh, Designing of experiments for evaluating the interactions of influencing factors on the photocatalytic activity of NiS and SnS_2: focus on coupling, supporting and nanoparticles, *J. Colloid Interface Sci.*, 2017, **490**, 628–641, DOI: 10.1016/j.jcis.2016.11.102.

14 Y. Yu, C. Zhao, X. Liu, M. Sui and Y. Meng, Selective flocculation of pollutants in wastewater using pH responsive HM-alginate/chitosan complexes, *J. Environ.*

Chem. Eng., 2017, **5**, 5406–5410, DOI: 10.1016/j.jece.2017.10.025.

15 H. Zhang, G. Xue, H. Chen and X. Li, Magnetic biochar catalyst derived from biological sludge and ferric sludge using hydrothermal carbonization: preparation, characterization and its circulation in Fenton process for dyeing wastewater treatment, *Chemosphere*, 2018, **191**, 64–71, DOI: 10.1016/j.chemosphere.2017.10.026.

16 M. Nasrollahzadeh, Z. Issaabadi and S. M. Sajadi, Green synthesis of a Cu/MgO nanocomposite by: *Cassytha filiformis* L. extract and investigation of its catalytic activity in the reduction of methylene blue, congo red and nitro compounds in aqueous media, *RSC Adv.*, 2018, **8**, 3723–3735, DOI: 10.1039/c7ra13491f.

17 H. Wang, J. Z. Xu, J. J. Zhu and H. Y. Chen, Preparation of CuO nanoparticles by microwave irradiation, *J. Cryst. Growth*, 2002, **244**, 88–94, DOI: 10.1016/S0022-0248(02)01571-3.

18 J. Cao, Y. Wang, T. Ma, Y. Liu and Z. Yuan, Synthesis of porous hematite nanorods loaded with CuO nanocrystals as catalysts for CO oxidation, *J. Nat. Gas Chem.*, 2011, **20**, 669–676, DOI: 10.1016/S1003-9953(10)60238-1.

19 J. Kaneshiro, N. Gaillard, R. Rocheleau and E. Miller, Advances in copper-chalcopyrite thin films for solar energy conversion, *Sol. Energy Mater. Sol. Cells*, 2010, **94**, 12–16, DOI: 10.1016/j.solmat.2009.03.032.

20 Y. Zhang, X. He, J. Li, H. Zhang and X. Gao, Gas-sensing properties of hollow and hierarchical copper oxide microspheres, *Sens. Actuators, B*, 2007, **128**, 293–298, DOI: 10.1016/j.snb.2007.06.013.

21 B. R. Huang, C. S. Yeh, D. C. Wang, J. T. Tan and J. Sung, Field emission studies of amorphous carbon deposited on copper nanowires grown by cathodic arc plasma deposition, *Xinxing Tan Cailiao*, 2009, **24**, 97–101, DOI: 10.1016/s1872-5805(08)60040-2.

22 N. Wongpisutpaisan, P. Charoonsuk, N. Vittayakorn and W. Pecharapa, Sonochemical synthesis and characterization of copper oxide nanoparticles, *Energy Procedia*, 2011, **9**, 404–409, DOI: 10.1016/j.egypro.2011.09.044.

23 M. Kaur, K. P. Muthe, S. K. Despande, S. Choudhury, J. B. Singh, N. Verma, S. K. Gupta and J. V Yakhmi, Growth and branching of CuO nanowires by thermal oxidation of copper, *J. Cryst. Growth*, 2006, **289**, 670–675, DOI: 10.1016/j.jcrysgro.2005.11.111.

24 M. H. Yamukyan, K. V Manukyan and S. L. Kharatyan, Copper oxide reduction by combined reducers under the combustion mode, *Chem. Eng. J.*, 2008, **137**, 636–642, DOI: 10.1016/j.cej.2007.05.033.

25 J. Zhu, D. Li, H. Chen, X. Yang, L. Lu and X. Wang, Highly dispersed CuO nanoparticles prepared by a novel quick-precipitation method, *Mater. Lett.*, 2004, **58**, 3324–3327, DOI: 10.1016/j.matlet.2004.06.031.

26 K. T. Karthikeyan, A. Nithya and K. Jothivenkatachalam, Photocatalytic and antimicrobial activities of chitosan-TiO_2 nanocomposite, *Int. J. Biol. Macromol.*, 2017, **104**, 1762–1773, DOI: 10.1016/j.ijbiomac.2017.03.121.

27 G. Rajakumar, A. A. Rahuman, S. M. Roopan, V. G. Khanna, G. Elango, C. Kamaraj, A. A. Zahir and K. Velayutham, Fungus-mediated biosynthesis and characterization of TiO_2 nanoparticles and their activity against pathogenic bacteria, *Spectrochim. Acta, Part A*, 2012, **91**, 23–29, DOI: 10.1016/j.saa.2012.01.011.

28 A. K. Jha, K. Prasad and A. R. Kulkarni, Synthesis of TiO_2 nanoparticles using microorganisms, *Colloids Surf., B*, 2009, **71**, 226–229, DOI: 10.1016/j.colsurfb.2009.02.007.

29 N. Arjunan, H. L. J. Kumari, C. M. Singaravelu, R. Kandasamy and J. Kandasamy, Physicochemical investigations of biogenic chitosan-silver nanocomposite as antimicrobial and anticancer agent, *Int. J. Biol. Macromol.*, 2016, **92**, 77–87, DOI: 10.1016/j.ijbiomac.2016.07.003.

30 A. M. Youssef, M. S. Abdel-Aziz and S. M. El-Sayed, Chitosan nanocomposite films based on Ag-NP and Au-NP biosynthesis by *Bacillus subtilis* as packaging materials, *Int. J. Biol. Macromol.*, 2014, **69**, 185–191, DOI: 10.1016/j.ijbiomac.2014.05.047.

31 A. Anitha, S. Sowmya, P. T. S. Kumar, S. Deepthi, K. P. Chennazhi, H. Ehrlich, M. Tsurkan and R. Jayakumar, Chitin and chitosan in selected biomedical applications, *Prog. Polym. Sci.*, 2014, **39**, 1644–1667, DOI: 10.1016/j.progpolymsci.2014.02.008.

32 I. Perelshtein, E. Ruderman, N. Perkas, T. Tzanov, J. Beddow, E. Joyce, T. J. Mason, M. Blanes, K. Mollá, A. Patlolla, A. I. Frenkel and A. Gedanken, Chitosan and chitosan-ZnO-based complex nanoparticles: formation, characterization, and antibacterial activity, *J. Mater. Chem. B*, 2013, **1**, 1968–1976, DOI: 10.1039/c3tb00555k.

33 S. Sathiyavimal, S. Vasantharaj, T. Kaliannan and A. Pugazhendhi, Eco-biocompatibility of chitosan coated biosynthesized copper oxide nanocomposite for enhanced industrial (Azo) dye removal from aqueous solution and antibacterial properties, *Carbohydr. Polym.*, 2020, **241**, 116243, DOI: 10.1016/j.carbpol.2020.116243.

34 R. C. F. Cheung, T. B. Ng, J. H. Wong and W. Y. Chan, *Chitosan: an update on potential biomedical and pharmaceutical applications*, 2015, DOI: 10.3390/md13085156.

35 J. M. F. Pavoni, N. Z. dos Santos, I. C. May, L. D. Pollo and I. C. Tessaro, Impact of acid type and glutaraldehyde crosslinking in the physicochemical and mechanical properties and biodegradability of chitosan films, *Polym. Bull.*, 2021, **78**, 981–1000, DOI: 10.1007/s00289-020-03140-4.

36 A. Arena, G. Scandurra and C. Ciofi, Copper oxide chitosan nanocomposite: characterization and application in non-enzymatic hydrogen peroxide sensing, *Sensors*, 2017, **17**(10), 2198, DOI: 10.3390/s17102198.

37 B. P. Singh, M. Chaudhary, A. Kumar, A. K. Singh, Y. K. Gautam, S. Rani and R. Walia, Effect of Co and Mn doping on the morphological, optical and magnetic properties of CuO nanostructures, *Solid State Sci.*, 2020, **106**, 106296, DOI: 10.1016/j.solidstatesciences.2020.106296.

38 A. ur Rehman, M. Aadil, S. Zulfiqar, P. O. Agboola, I. Shakir, M. F. Aly Aboud, S. Haider and M. F. Warsi, Fabrication of

binary metal doped CuO nanocatalyst and their application for the industrial effluents treatment, *Ceram. Int.*, 2021, **47**, 5929–5937, DOI: **10.1016/j.ceramint.2020.11.064**.

39 K. Phiwdang, S. Suphankij, W. Mekprasart and W. Pecharapa, Synthesis of CuO nanoparticles by precipitation method using different precursors, *Energy Procedia*, 2013, **34**, 740–745, DOI: **10.1016/j.egypro.2013.06.808**.

40 M. Ikram, S. Hayat, M. Imran, A. Haider, S. Naz, A. Ul-Hamid, I. Shahzadi, J. Haider, A. Shahzadi, W. Nabgan and S. Ali, Novel Ag/cellulose-doped CeO_2 quantum dots for efficient dye degradation and bactericidal activity with molecular docking study, *Carbohydr. Polym.*, 2021, **269**, 118346, DOI: **10.1016/j.carbpol.2021.118346**.

41 S. Shaheen, A. Iqbal, M. Ikram, K. Ul-Ain, S. Naz, A. Ul-Hamid, A. Shahzadi, A. Haider, W. Nabgan and J. Haider, Effective Disposal of Methylene Blue and Bactericidal Benefits of Using GO-Doped MnO_2 Nanorods Synthesized through One-Pot Synthesis, *ACS Omega*, 2021, **6**, 24866–24878, DOI: **10.1021/acsomega.1c03723**.

42 S. Ossama, A. Ahmad, M. Ikram, M. Imran and S. Naz, Novel prism shaped C_3N_4-doped Fe@Co_3O_4 nanocomposites and their dye degradation and bactericidal potential with molecular docking study, *RSC Adv.*, 2021, **11**, 23330–23344, DOI: **10.1039/d1ra03949k**.

43 A. Ashfaq, M. Ikram, A. Haider, A. U. Hamid, I. Shahzadi and J. Haider, Nitrogen and Carbon Nitride – Doped – for Multiple Catalysis and Its Antimicrobial Activity, *Nanoscale Res. Lett.*, 2021, **16**, 119, DOI: **10.1186/s11671-021-03573-4**.

44 M. Figiela, M. Wysokowski, M. Galinski, T. Jesionowski and I. Stepniak, Synthesis and characterization of novel copper oxide-chitosan nanocomposites for non-enzymatic glucose sensing, *Sens. Actuators, B*, 2018, **272**, 296–307, DOI: **10.1016/j.snb.2018.05.173**.

45 R. Rajendran, K. Varadharajan and V. Jayaraman, Fabrication of tantalum doped CdS nanoparticles for enhanced photocatalytic degradation of organic dye under visible light exposure, *Colloids Surf., A*, 2019, **580**, 123688, DOI: **10.1016/j.colsurfa.2019.123688**.

46 S. M. Selvan, K. V. Anand, K. Govindaraju, S. Tamilselvan and V. G. Kumar, Green synthesis of copper oxide nanoparticles and mosquito larvicidal activity against dengue, zika and chikungunya causing vector Aedes aegypti, *IET Nanobiotechnol.*, 2018, **12**(8), 1042–1046.

47 A. S. Ethiraj and D. J. Kang, Synthesis and characterization of CuO nanowires by a simple wet chemical method, *Nanoscale Res. Lett.*, 2012, **7**, 1–5, DOI: **10.1186/1556-276X-7-70**.

48 H. C. A. Murthy, T. Desalegn, M. Kassa, B. Abebe and T. Assefa, Synthesis of Green Copper Nanoparticles Using Medicinal Plant Hagenia abyssinica (Brace) JF. Gmel. Leaf Extract: Antimicrobial Properties, *J. Nanomater.*, 2020, **2020**, 3924081, DOI: **10.1155/2020/3924081**.

49 C. Tamuly, I. Saikia, M. Hazarika and M. R. Das, Reduction of aromatic nitro compounds catalyzed by biogenic CuO nanoparticles, *RSC Adv.*, 2014, **4**, 53229–53236, DOI: **10.1039/c4ra10397a**.

50 P. K. Raul, S. Senapati, A. K. Sahoo, I. M. Umlong, R. R. Devi, A. J. Thakur and V. Veer, CuO nanorods: a potential and efficient adsorbent in water purification, *RSC Adv.*, 2014, **4**, 40580–40587, DOI: **10.1039/c4ra04619f**.

51 W. Tan, Q. Li, F. Dong, J. Zhang, F. Luan, L. Wei, Y. Chen and Z. Guo, Novel cationic chitosan derivative bearing 1,2,3-triazolium and pyridinium: Synthesis, characterization, and antifungal property, *Carbohydr. Polym.*, 2018, **182**, 180–187, DOI: **10.1016/j.carbpol.2017.11.023**.

52 N. H. Rezazadeh, F. Buazar and S. Matroodi, Synergistic effects of combinatorial chitosan and polyphenol biomolecules on enhanced antibacterial activity of bifunctionalized silver nanoparticles, *Sci. Rep.*, 2020, **10**, 1–13, DOI: **10.1038/s41598-020-76726-7**.

53 A. Tadjarodi, O. Akhavan and K. Bijanzad, Photocatalytic activity of CuO nanoparticles incorporated in mesoporous structure prepared from bis(2-aminonicotinato) copper(II) microflakes, *Trans. Nonferrous Met. Soc. China*, 2015, **25**, 3634–3642, DOI: **10.1016/S1003-6326(15)64004-3**.

54 P. L. Holland and W. B. Tolman, Three-coordinate Cu(II) complexes: structural models of trigonal-planar type 1 copper protein active sites, *J. Am. Chem. Soc.*, 1999, **121**, 7270–7271, DOI: **10.1021/ja991533e**.

55 S. Logpriya, V. Bhuvaneshwari, D. Vaidehi, R. P. SenthilKumar, R. S. Nithya Malar, B. Pavithra Sheetal, R. Amsaveni and M. Kalaiselvi, Preparation and characterization of ascorbic acid-mediated chitosan–copper oxide nanocomposite for antimicrobial, sporicidal and biofilm-inhibitory activity, *J. Nanostruct. Chem.*, 2018, **8**, 301–309, DOI: **10.1007/s40097-018-0273-6**.

56 A. M. Raba-Páez, J. O. D. Malafatti, C. A. Parra-Vargas, E. C. Paris and M. Rincón-Joya, Effect of tungsten doping on the structural, morphological and bactericidal properties of nanostructured CuO, *PLoS One*, 2020, **15**, 1–16, DOI: **10.1371/journal.pone.0239868**.

57 P. Kumar, M. Chandra Mathpal, J. Prakash, B. C. Viljoen, W. D. Roos and H. C. Swart, Band gap tailoring of cauliflower-shaped CuO nanostructures by Zn doping for antibacterial applications, *J. Alloys Compd.*, 2020, **832**, 154968, DOI: **10.1016/j.jallcom.2020.154968**.

58 M. Ponnar, C. Thangamani, P. Monisha, S. S. Gomathi and K. Pushpanathan, Influence of Ce doping on CuO nanoparticles synthesized by microwave irradiation method, *Appl. Surf. Sci.*, 2018, **449**, 132–143, DOI: **10.1016/j.apsusc.2018.01.126**.

59 Y. Wang, T. Jiang, D. Meng, J. Kong, H. Jia and M. Yu, Controllable fabrication of nanostructured copper compound on a Cu substrate by a one-step route, *RSC Adv.*, 2015, **5**, 16277–16283, DOI: **10.1039/c4ra14523b**.

60 P. Chand, A. Gaur and A. Kumar, Structural, optical and ferroelectric behavior of CuO nanostructures synthesized at different pH values, *Superlattices Microstruct.*, 2013, **60**, 129–138, DOI: **10.1016/j.spmi.2013.04.026**.

61 M. Hellwig, A. Milanov, D. Barreca, J. L. Deborde, R. Thomas, M. Winter and A. Devi, Stabilization of amide-based complexes of niobium and tantalum using malonates as chelating ligands: precursor chemistry and thin film

deposition, *Chem. Mater.*, 2007, **19**, 6077–6087, DOI: 10.1021/cm0630441.

62 P. M. L. Perez, R. M. P. Silva, C. Serra, I. Pashkuleva and R. L. Reis, Surface phosphorylation of chitosan significantly improves osteoblast cell viability, attachment and proliferation, *J. Mater. Chem.*, 2010, **20**, 483–491, DOI: 10.1039/B911854C.

63 R. Simpson, R. G. White, J. F. Watts and M. A. Baker, XPS investigation of monatomic and cluster argon ion sputtering of tantalum pentoxide, *Appl. Surf. Sci.*, 2017, **405**, 79–87, DOI: 10.1016/j.apsusc.2017.02.006.

64 D. A. Svintsitskiy, T. Y. Kardash, O. A. Stonkus, E. M. Slavinskaya, A. I. Stadnichenko, S. V. Koscheev and A. I. Boronin, In situ XRD, XPS, TEM, and TPR study of highly active in CO oxidation CuO nanopowders, *J. Phys. Chem. C*, 2013, **117**, 14588–14599, DOI: 10.1021/jp403339r.

65 M. Ikram, T. Inayat, A. Haider, A. U. Hamid, J. Haider, W. Nabgan, A. Saeed, A. Shahbaz and S. Hayat, Graphene Oxide – Doped MgO Nanostructures for Highly Efficient Dye Degradation and Bactericidal Action, *Nanoscale Res. Lett.*, 2021, **16**, 56, DOI: 10.1186/s11671-021-03516-z.

66 J. P. Perdew, K. Burke and M. Ernzerhof, Generalized Gradient Approximation Made Simple, *Phys. Rev. Lett.*, 1996, **77**(18), 3865, DOI: 10.1103/PhysRevLett.77.3865.

67 S. Smidstrup, *et al.*, QuantumATK: an integrated platform of electronic and atomic-scale modelling tools, *J. Phys.: Condens. Matter*, 2020, **32**(1), 015901, DOI: 10.1088/1361-648X/AB4007.

68 M. J. van Setten, M. Giantomassi, E. Bousquet, M. J. Verstraete, D. R. Hamann, X. Gonze and G.-M. Rignanese, *The PseudoDojo: training and grading a 85 element optimized norm-conserving pseudopotential table*, Elsevier, 2021, vol. 226, pp. 39–54.

69 A. K. Mishra, A. Roldan and N. H. de Leeuw, CuO Surfaces and CO_2 Activation: A Dispersion-Corrected DFT+U Study, *J. Phys. Chem. C*, 2016, **120**, 2198–2214.

70 W. Khan, S. Azam, M. B. Kanoun and S. Goumri-Said, Optoelectronic structure and related transport properties of BiCuSeO based oxychalcogenides: first principle calculations, *Solid State Sci.*, 2016, **58**, 86–93.

71 F. Ahmad, M. K. Agusta, R. Maezono and H. K. Dipojono, DFT + U study of H_2O adsorption and dissociation on stoichiometric and nonstoichiometric CuO(1 1 1) surfaces, *J. Phys.: Condens. Matter*, 2020, **32**, 045001.

72 J. Hassan, *et al.*, h-BN nanosheets doped with transition metals for environmental remediation; a DFT approach and molecular docking analysis, *Mater. Sci. Eng., B*, 2021, **272**, 115365, DOI: 10.1016/J.MSEB.2021.115365.

73 M. B Kanoun and L. Cavallo, Quantifying the Impact of Relativity and of Dispersion Interactions on the Activation of Molecular Oxygen Promoted by Noble Metal Nanoparticles, *J. Phys. Chem. C*, 2014, **118**, 13707–13714.